Editors' Suggestion

Experimental Observation of Momentum-Space Chiral Edge Currents in Room-Temperature Atoms

Han Cai,[1] Jinhong Liu,[1,2] Jinze Wu,[1,2] Yanyan He,[1] Shi-Yao Zhu,[1,3] Jun-Xiang Zhang,[1,*] and Da-Wei Wang[1,4,†]

[1]*Interdisciplanery Center for Quantum Information, Department of Physics and State Key Laboratory of Modern Optical Instrumentation, Zhejiang University, Hangzhou 310027, China*

[2]*State Key Laboratory of Quantum Optics and Quantum Optics Devices, Institute of Opto-Electronics, Shanxi University, Taiyuan 030006, China*

[3]*Synergetic Innovation Center of Quantum Information and Quantum Physics, University of Science and Technology of China, Hefei, Anhui 230026, China*

[4]*CAS Center of Excellence in Topological Quantum Computation, University of Chinese Academy of Sciences, Beijing 100190, China*

(Received 30 August 2018; published 14 January 2019)

Chiral edge currents play an important role in characterizing topological matter. In atoms, they have been observed at such a low temperature that the atomic motion can be measured. Here we report the first experimental observation of chiral edge currents in atoms at room temperature. Staggered magnetic fluxes are induced by the spatial phase difference between two standing-wave light fields, which couple atoms to form a momentum-space zigzag superradiance lattice. The chiral edge currents are measured by comparing the directional superradiant emissions of two timed Dicke states in the lattice. Our results pave the way for simulating topological physics in hot atoms.

DOI: 10.1103/PhysRevLett.122.023601

The quantum Hall effect [1] reveals a topological class of matter that is characterized by the Chern numbers of energy bands [2]. The chiral edge currents located at the boundaries of two bulk materials with different Chern numbers are usually measured to investigate the band topology. The chirality of the edge currents is featured by the locking between the direction of the currents and the (pseudo)spin states of the edge excitations [3,4]. The chirality is robust against local perturbations and only changes when the energy bands go through a topological transition. Since the edges have a lower dimension than the bulk, the edge currents provide a convenient platform to investigate topological physics in a higher dimension, such as the quantum Hall effect in four dimensions [5,6]. The chirality of the edge currents persists even when a two-dimensional lattice is reduced to quasi-one-dimensional ribbons [7], which has been experimentally demonstrated with ultracold fermions [8,9] and bosons [10,11]. In those experiments, the chiral edge currents were measured with the atomic motions and thus were only observed at a low temperature, where the thermal motions are negligible.

Here we report the experimental observation of the momentum-space chiral edge currents in a superradiance lattice [12–14] of cesium atoms at room temperature. The zigzag lattice that we have synthesized is similar to the ladder structures in the experiments with cold atoms [7,8,11] and is currently under intensive investigation [15–18]. Different from the momentum-space lattices characterized by the recoil momentum of cold atoms [17,19], the superradiance lattice is a momentum-space lattice composed by the timed Dicke states [20] [see Eq. (3)], which are collective atomic excitations with phase correlations. The phase correlations can be understood as the momenta of the collective excitations, which have directional superradiant light emissions when they satisfy the phase-matching condition with a light mode [20]. A remarkable advantage of our approach is that the edge currents are observed at room temperature. Instead of measuring the atomic motions [8–11], the chiral edge currents are measured by comparing the directional light emissions from two timed Dicke states. Our study has substantially lowered the threshold of the experimental observation of chiral edge currents in atoms.

To highlight the physics, we introduce our basic model with Λ-type three-level atoms as shown in Fig. 1(a). An excited state $|b\rangle$ and a metastable state $|a\rangle$ are coupled by two standing waves with different frequencies, i.e., a near-resonant and a far-detuned standing wave with field amplitude envelopes $\cos(k_c x)$ and $\cos(k_c x + \phi/2)$, where $\phi/2$ is their spatial phase difference and k_c is the $\hat{x}$ component of the light wave vector. The detuning between the two standing-wave coupling fields is small enough such that the difference between the amplitudes of their wave vectors k_c can be neglected. A probe field couples the ground state $|c\rangle$ to $|b\rangle$. The Hamiltonian is (we set $\hbar = 1$)

 © 2019 American Physical Society

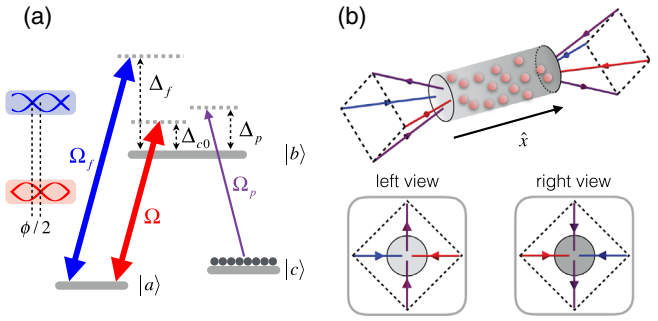

FIG. 1. Schematic configuration of the experiment. (a) Atomic levels and the near-resonant and far-detuned standing-wave coupling fields with a relative spatial phase difference $\phi/2$. (b) The configuration of the lasers. The probe and its reflected fields (purple), the far-detuned (blue) and near-resonant (red) standing-wave coupling fields form a box configuration in order to satisfy the phase-matching condition.

$$H=\sum_m\left[\frac{\Delta_c}{2}+2\kappa\cos(2k_cx+\phi)\right](|a_m\rangle\langle a_m|-|b_m\rangle\langle b_m|)+\sum_m 2\Omega\cos(k_cx_m)(|b_m\rangle\langle a_m|+\text{H.c.})+\sum_m(\Omega_p e^{ik_px_m}e^{-i[\Delta_p-(\nu_c-\omega_{ba})/2]t}|b_m\rangle\langle c_m|+\text{H.c.}),\quad(1)$$

where $\Delta_c=\Delta_{c0}+4\kappa$ with $\Delta_{c0}=\nu_c-\omega_{ba}$ being the detuning of the near-resonant coupling field frequency ν_c from the atomic transition between $|b\rangle$ and $|a\rangle$. ω_{ba} is the bare transition frequency and 4κ is a spatially homogeneous Stark shift induced by the far-detuned coupling fields, which also induce a spatially periodic Stark shift $2\kappa\cos(2k_cx+\phi)$. Here, $\kappa=\Omega_f^2/\Delta_f$, with Ω_f and $\Delta_f=\nu_f-\omega_{ba}$ being the Rabi frequency and detuning of each plane wave component of the far-detuned coupling field. $\Delta_p=\nu_p-\omega_{bc}$ is the detuning of the probe field frequency ν_p from the atomic transition frequency ω_{bc} between $|b\rangle$ and $|c\rangle$. Ω is the Rabi frequency of each plane wave component of the near-resonant coupling field. k_p is the $\hat{x}$ component of the probe field wave vector and x_m is the $\hat{x}$-axis coordinate of the mth atom. The derivation of the Hamiltonian in Eq. (1) can be found in the Supplemental Material [21].

By introducing collective atomic excitation operators $\hat{b}_j^\dagger=1/\sqrt{N}\sum_m e^{i(k_p+2jk_c)x_m}|b_m\rangle\langle c_m|$ and $\hat{a}_j^\dagger=1/\sqrt{N}\sum_m e^{i[k_p+(2j-1)k_c]x_m}|a_m\rangle\langle c_m|$, we transform the Hamiltonian to momentum space, $H=H_s+H_p$, where

$$H_s=\sum_j\Delta_c(\hat{a}_j^\dagger\hat{a}_j-\hat{b}_j^\dagger\hat{b}_j)/2+\sum_j[\Omega(\hat{a}_j^\dagger\hat{b}_j+\hat{a}_j^\dagger\hat{b}_{j-1})+e^{i\phi}\kappa(\hat{a}_j^\dagger\hat{a}_{j-1}-\hat{b}_j^\dagger\hat{b}_{j-1})+\text{H.c.}],\quad(2)$$

and $H_p=\sqrt{N}\Omega_p(\hat{b}_0^\dagger e^{-i[\Delta_p-(\nu_c-\omega_{ba})/2]t}+\text{H.c.})$. With the condition that $\Omega\gg\Omega_p$, most of the atoms are in the ground state $|c\rangle$, and $\hat{a}_j^\dagger$ and $\hat{b}_j^\dagger$ are approximately bosonic creation operators [12,23]. For single excitations, Eq. (2) is a Hamiltonian of a tight-binding superradiance lattice composed by timed Dicke states,

$$|B_j\rangle\equiv\hat{b}_j^\dagger|G\rangle=\frac{1}{\sqrt{N}}\sum_m e^{i(k_p+2jk_c)x_m}|c_1,\ldots,b_j,\ldots,c_N\rangle,\quad(3)$$

and $|A_j\rangle\equiv\hat{a}_j^\dagger|G\rangle$, with $|G\rangle=|c_1,c_2,\ldots,c_N\rangle$ being the ground state. The timed Dicke states $|B_j\rangle$ and $|A_j\rangle$ are phase-correlated collective excited states that contain a single excitation. The term "timed" indicates the phase correlations that show the timing of the excitations in the original scheme of Scully *et al.* [20]. For more excitations, as long as the excitation number is much less than the atomic number and there is no interaction between atoms, the physics remains the same due to the bosonic nature of the excitations.

Each up and down triangle encloses an effective magnetic flux ϕ and $\pi-\phi$, respectively, as shown in Fig. 2(a). We diagonalize H_s in real space,

$$H_s=h\mathbf{n}\cdot\boldsymbol{\sigma},\quad(4)$$

where $\mathbf{n}=(h_x\hat{x}+h_z\hat{z})/h$, with $h_x=2\Omega\cos(k_cx)$, $h_z=\Delta_c/2+2\kappa\cos(2k_cx+\phi)$, and $h=\sqrt{h_z^2+h_x^2}$. $\boldsymbol{\sigma}=\sum_{j=x,y,z}\sigma^j\hat{j}$ is the vector of the Pauli matrices of the pseudo-spin-up state $|a\rangle$ and pseudo-spin-down state $|b\rangle$. The dispersion relations in the upper and lower bands are $E_u=h$ and $E_l=-h$ with the eigenstates $|\psi_u\rangle=\cos(\theta/2)|a\rangle+\sin(\theta/2)|b\rangle$ and $|\psi_l\rangle=-\sin(\theta/2)|a\rangle+\cos(\theta/2)|b\rangle$, where θ is the polar angle of $\mathbf{n}$. In Fig. 2(b), we plot the dispersion (eigenenergy as a function of the position) with the "spin texture" $\langle\sigma^z\rangle$ denoted by the color. An interesting correlation between the dispersion and $\langle\sigma_z\rangle$ can be easily noticed from the case when $\phi=\pi/2$. The eigenstates that have a positive (negative) dispersion concentrate on the $|a\rangle$ ($|b\rangle$) edge.

The evolution of the momentum is determined by the dispersion relation in Fig. 2(b), $\partial p/\partial t=-\partial E/\partial x$ [12]. For example, when $\phi=\pi/2$ and near the zero eigenenergy, the momentum of an excitation created on the $|b\rangle$ sublattice increases with time (note the negative derivative of the red line), while on the $|a\rangle$ sublattice the momentum decreases. This is the essence of chiral edge currents; i.e., excitations on different edges or with different spin states move in opposite directions. To quantitatively clarify this feature, we define the chiral edge currents on the $|b\rangle$ sublattice as [7]

$$J_b(E)=-\sum_{i=u,l}\int dx\delta(E_i-E)|\langle\psi_i|b\rangle|^2\frac{\partial E_i}{\partial x},\quad(5)$$

where $\delta(E_i-E)$ is the Dirac delta function. $J_b(E)$ characterizes the dynamics of the total momentum of

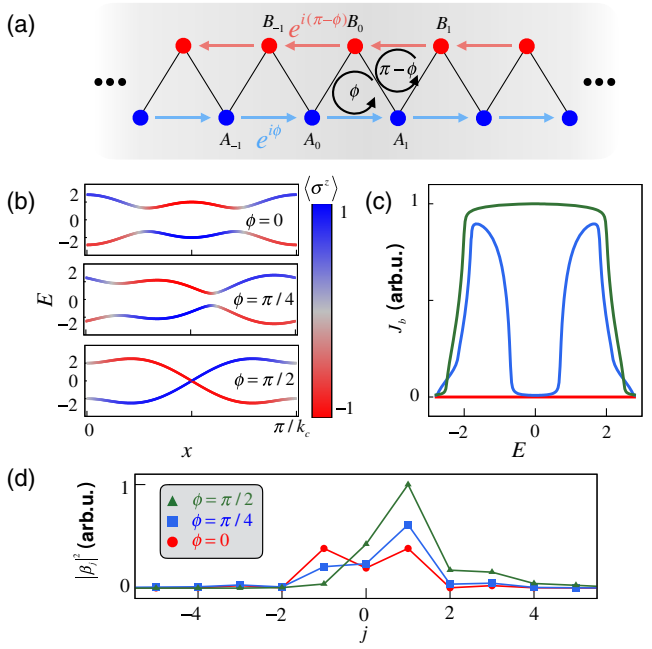

FIG. 2. Band structure and chiral edge currents of superradiance lattices with different magnetic fluxes. (a) The tight-binding lattice of the Hamiltonian H_s in Eq. (2). The red and blue arrows show the phase factors ϕ attached with the corresponding transitions. The total phases enclosed by the loop transitions in the up and down triangles are ϕ and $\pi-\phi$, respectively. (b) The dispersion relation according to Eq. (4) with $\phi=0$, $\pi/4$, and $\pi/2$. The color shows the $\langle\sigma_z\rangle$ of eigenstates and indicates which edge the eigenstates mainly locate on. (c) $J_b(E)$ in Eq. (5) for $\phi=0$ (red line), $\pi/4$ (blue line), and $\pi/2$ (green line). (d) The steady state distribution of the population $|\beta_j|^2$ in the $|b\rangle$ sublattice with a probe field pumping the atoms to the site $j=0$. The points are simply connected for clarity. The decoherence rates of states $|b\rangle$ and $|a\rangle$ are $\gamma_{bc}=1$ and $\gamma_{ac}=0.1$. The probe detuning $\Delta_p=0$. $\Omega=1$, $\kappa=1$, and $\Delta_c=0$. For $\phi=0$ and $\pi/4$, the lattice can still be excited in the gap ($\Delta_p=0$) due to a finite γ_{bc}.

excitations with energy E on the $|b\rangle$ sublattice. We can define a similar quantity for the $|a\rangle$ sublattice. However, we only focus on $J_b(E)$ since the probe field couples atoms to the $|b\rangle$ state. In Fig. 2(c), we notice that the sign of $J_b(E)$ does not change with E for a fixed ϕ. The sign becomes negative when $\phi>\pi$ (see the Supplemental Material [21]).

To generate $J_b(E)$, we apply a weak probe field with detuning $\Delta_p=E+(\nu_c-\omega_{ba})/2$ to pump the atoms from the ground state to the state $|B_0\rangle$. The momentum of the excitation moves in the direction determined by the sign of $J_b(E)$ and is finally balanced by the decoherence. In the steady state, the population distribution is plotted in Fig. 2(d). We define β_j as the probability amplitude of the state $|B_j\rangle$. For $\phi=0$, the distribution of $|\beta_j|^2$ is symmetric on the two sides of $|B_0\rangle$, in contrast to the asymmetric distribution when $\phi=\pi/4$ and $\pi/2$, where the population is biased to $j>0$ due to a positive $J_b(E)$.

In the experiment, we detect the superradiant emissions of two specific timed Dicke states to show the edge currents. The timed Dicke states with a phase correlation that matches the wave vectors of the light in the medium, i.e., $|k_p+2jk_c|\approx|k_p|$, have directional superradiant emissions [20]. In the current scheme where $|a\rangle$ and $|c\rangle$ are nearly degenerate, the timed Dicke state $|B_{-1}\rangle$ (or $|B_{+1}\rangle$) is the only superradiant state besides $|B_0\rangle$ for a probe light incident along $+\hat{x}$ (or $-\hat{x}$). The radiation from these two superradiant states can be considered as the reflections of the probe fields. We define $R_\pm$ as the reflectivities of the probe fields incident along the $\pm\hat{x}$ axis. The relationship between $R_\pm$ and $\beta_{\pm1}$ is (see the Supplemental Material [21])

$$\frac{R_+}{R_-}=\frac{|\beta_{-1}|^2}{|\beta_{+1}|^2}. \tag{6}$$

This relation is independent of the density of the atoms, the length of the vapor cell, and the phase mismatch.

We have used the $D1$ line of cesium atoms in the experiment: $|a\rangle=|6^2S_{1/2},F=3\rangle$, $|b\rangle=|6^2P_{1/2},F=4\rangle$, and $|c\rangle=|6^2S_{1/2},F=4\rangle$ (see Supplemental Material [21]). Typical experimental results are shown in Fig. 3. The reflection spectra depend on the phase ϕ. Only when $\phi=0$ and π, we observe $R_+=R_-$. For $0<\phi<\pi$, we observe $R_+<R_-$, which indicates a larger population in $|B_{+1}\rangle$ than in $|B_{-1}\rangle$, resulted from an edge current propagating along $+\hat{x}$. In contrast, we observe $R_+>R_-$ for $\pi<\phi<2\pi$, which indicates an edge current along $-\hat{x}$. The difference R_--R_+ demonstrates the overall edge current $\bar{J}_b=\int dEJ_b(E)/2h_{\max}$ with $h_{\max}$ being the maximum eigenenergy, as shown in Fig. 3(b).

In the following, we analyze the robustness of the edge currents against thermal motions. From Fig. 3(a), we see that the reflection spectra are not Doppler broadened. The nonzero region of the spectra coincides with the energy bands of the superradiance lattice. Their scales are both around 30 MHz. This feature of standing-wave coupled electromagnetically induced transparency was already found by Feldman and Feld in 1972 [24]. To understand this, we notice that the atoms that have a Doppler shift larger than the bandwidth are out of resonance with the probe field no matter their positions, such that they cannot be excited. For atoms with Doppler shift smaller than the lattice bandwidth, they move in the real-space Brillouin zone and their contribution to the edge currents needs to be averaged with their positions. The chiral edge currents induce a difference between the two reflectivities, $R_d\equiv R_--R_+\propto|\langle\beta_{+1}\rangle|^2-|\langle\beta_{-1}\rangle|^2$, where $\langle\rangle$ is the average over the Doppler shifts due to the thermal motions of the atoms. To quantify the effect of the chiral edge currents on the whole reflection spectra, we take an average of R_d,

$$\bar{R}_d=\frac{1}{F}\int R_d d\Delta_p, \tag{7}$$

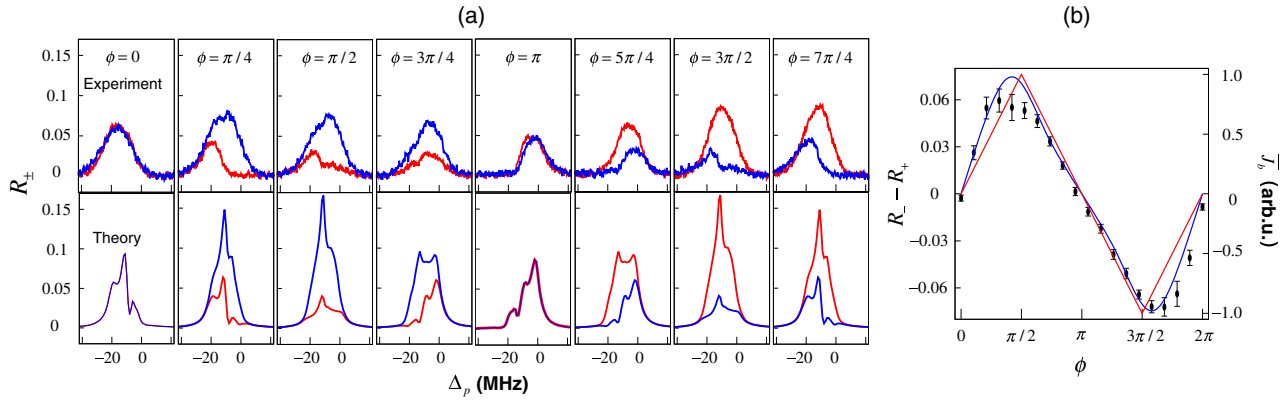

FIG. 3. Chiral edge currents demonstrated by the reflection spectra. (a) The reflectivities R_+ (red lines) and R_- (blue lines) with different phases. (b) $R_- - R_+$ at the center of the spectrum $\Delta_p = -11(\pm 1)$ MHz (similar results at other detunings) versus the phase ϕ (dots with error bars, experimental results of ten sets of data; blue line, numerical simulation), compared with the overall chiral edge current $\bar{J}_b$ (red line). The power of each plane wave component of the near-resonant coupling field is 6.5 mW with an effective Rabi frequency $\Omega = 5.5$ MHz. The power of each plane wave component of the far-detuned coupling field is 120 mW with an effective Rabi frequency $\Omega_f = 33.3$ MHz and a detuning $\Delta_f = 200$ MHz. $\kappa = 5.5$ MHz. $\Delta_c = 1.0$ MHz. The power of each probe beam is 20 μW. We have used $\gamma_{bc} = 2.3$ MHz and $\gamma_{ac} = 0.95$ MHz in the numerical simulation. The differences between the simulation and experiment are attributed to slight asymmetry in the optical alignment, an average of ϕ along the vapor cell ($\Delta\phi \approx 0.05\pi$), and the Gaussian rather than plane wave profiles of the coupling fields.

where $F = 40$ MHz is the frequency range of an integration from -30 to 10 MHz in the reflection spectra. In Fig. 4, we show the experimental data and numerical simulation of $\bar{R}_d$ as functions of Δ_c and ϕ. For an on-site potential difference $\Delta_c \approx 0$, $\bar{R}_d$ is approximately a sinusoidal function of the phase ϕ. This means our method can be used to measure a phase difference between two standing waves. For Δ_c larger than the bandwidth, the interedge transitions are inhibited and the effect of the synthetic magnetic field diminishes due to the inefficient loop transitions. As a result, $\bar{R}_d$ decreases rapidly to zero when Δ_c increases. The results in Fig. 4 can be understood as the phase diagram of an extended Haldane model [7], and its relation to the dynamic classification of topological phases [25] will be discussed elsewhere.

The results reported here are substantially different from the temperature-independent edge currents in the photonic lattices [26–31], where the propagation of the photons governed by the Maxwell equations is made analogous to the Schrödinger equation [32]. The edge states there are photonic states rather than atomic states. The temperature has no influence on the photons. In our current study, the topological bands are for the atoms and they intrinsically obey the Schrödinger equation. The thermal motions of the atoms make a convenient average of the edge currents. In addition, our lattice is in momentum space, in contrast to the real-space topological photonic lattices. Although the edge currents are detected by light in our experiment, they are currents of collective excitations of atoms in momentum space, not light in real space.

On the other hand, our results are closely related to the spin-orbit coupled system [33,34] and the momentum-space lattice [17,19] in cold atoms, with the difference that the momentum is represented by the phase correlation of the collective excitation, instead of the recoil momentum, which is negligible in our study. An extension of our model to higher dimensions [13] can be used to simulate the Haldane model [35,36] and the two-dimensional spin-orbit coupling [33,34]. By using Rydberg states [37,38] we can introduce interactions between the excitations and study the many-body

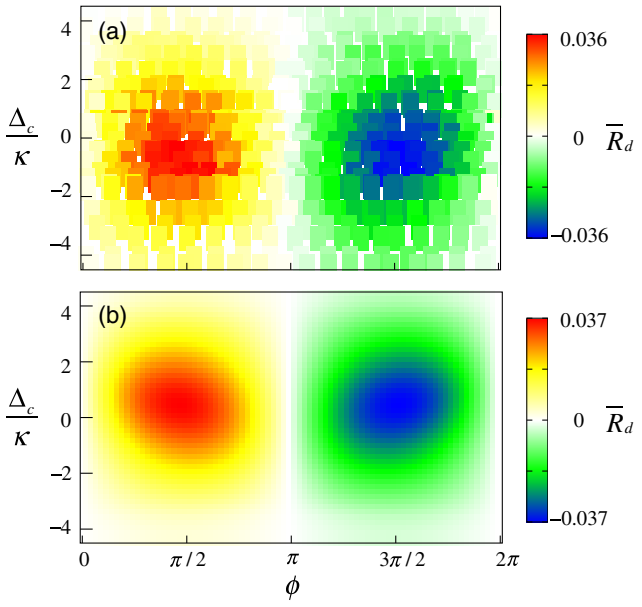

FIG. 4. Averaged difference between the two reflectivities in Eq. (7). (a) Experimental data. (b) Numerical simulation. The parameters are the same as in Fig. 3.

effect in flux lattices [39]. An interesting connection of our results can also be made to the unidirectional reflectionless (invisible) photonic structures [40–43], such as the parity-time symmetric materials [44]. We have observed that under certain conditions one of the two reflectivities is nearly zero while the other is big. Another observation is that the transmissions of the probe fields in the two opposite directions are the same, although the transmissions are phase dependent. This is because our system does not break the time-reversal symmetry. It is interesting to note that an effective magnetic field in momentum space does not result in optical nonreciprocity, while an effective electric field in momentum space can break the time-reversal symmetry and induce optical nonreciprocity [45]. Our study provides a new way to measure the spatial relative phase between two light fields that have different frequencies. The phase information is converted to intensity signals. This can be used in phase-contrast microscopy.

We thank B. Gadway, J. Q. You, and G. Juzeliunas for fruitful discussion, and Zhiguo Wang for technical support. We acknowledge the support from National Natural Science Foundation of China (No. 91736209), National Natural Science Foundation of China (No. 11874322 and No. 11574188), the National Key Research and Development Program of China (Grants No. 2017YFA0304202 and No. 2018YFA0307200). D.-W. W. was also supported by the Key Research Program of the Chinese Academy of Sciences (Grant No. XDPB08-3).

*junxiang_zhang@zju.edu.cn
†dwwang@zju.edu.cn

[1] K. von Klitzing, G. Dorda, and M. Pepper, New Method for High-Accuracy Determination of the Fine-Structure Constant Based on Quantized Hall Resistance, Phys. Rev. Lett. **45**, 494 (1980).
[2] D. J. Thouless, M. Kohmoto, M. P. Nightingale, and M. Dennijs, Quantized Hall Conductance in a Two-Dimensional Periodic Potential, Phys. Rev. Lett. **49**, 405 (1982).
[3] C. L. Kane and E. J. Mele, Quantum Spin Hall Effect in Graphene, Phys. Rev. Lett. **95**, 226801 (2005).
[4] B. A. Bernevig and S.-C. Zhang, Quantum Spin Hall Effect, Phys. Rev. Lett. **96**, 106802 (2006).
[5] M. Lohse, C. Schweizer, H. M. Price, O. Zilberberg, and I. Bloch, Exploring 4d quantum Hall physics with a 2d topological charge pump, Nature (London) **553**, 55 (2018).
[6] O. Zilberberg, S. Huang, J. Guglielmon, M. Wang, K. P. Chen, Y. E. Kraus, and M. C. Rechtsman, Photonic topological boundary pumping as a probe of 4d quantum Hall physics, Nature (London) **553**, 59 (2018).
[7] D. Hügel and B. Paredes, Chiral ladders and the edges of quantum Hall insulators, Phys. Rev. A **89**, 023619 (2014).
[8] M. Mancini, G. Pagano, G. Cappellini, L. Livi, M. Rider, J. Catani, C. Sias, P. Zoller, M. Inguscio, M. Dalmonte, and L. Fallani, Observation of chiral edge states with neutral fermions in synthetic Hall ribbons, Science **349**, 1510 (2015).
[9] L. F. Livi, G. Cappellini, M. Diem, L. Franchi, C. Clivati, M. Frittelli, F. Levi, D. Calonico, J. Catani, M. Inguscio, and L. Fallani, Synthetic Dimensions and Spin-Orbit Coupling with an Optical Clock Transition, Phys. Rev. Lett. **117**, 220401 (2016).
[10] M. Atala, M. Aidelsburger, M. Lohse, J. T. Barreiro, B. Paredes, and I. Bloch, Observation of chiral currents with ultracold atoms in bosonic ladders, Nat. Phys. **10**, 588 (2014).
[11] B. K. Stuhl, H.-I. Lu, L. M. Aycock, D. Genkina, and I. B. Spielman, Visualizing edge states with an atomic Bose gas in the quantum Hall regime, Science **349**, 1514 (2015).
[12] D.-W. Wang, R.-B. Liu, S.-Y. Zhu, and M. O. Scully, Superradiance Lattice, Phys. Rev. Lett. **114**, 043602 (2015).
[13] D.-W. Wang, H. Cai, L. Yuan, S.-Y. Zhu, and R.-B. Liu, Topological phase transitions in superradiance lattices, Optica **2**, 712 (2015).
[14] L. Chen, P. Wang, Z. Meng, L. Huang, H. Cai, D.-W. Wang, S.-Y. Zhu, and J. Zhang, Experimental Observation of One-Dimensional Superradiance Lattices in Ultracold Atoms, Phys. Rev. Lett. **120**, 193601 (2018).
[15] E. Anisimovas, M. Račiūnas, C. Sträter, A. Eckardt, I. B. Spielman, and G. Juzeliūnas, Semisynthetic zigzag optical lattice for ultracold bosons, Phys. Rev. A **94**, 063632 (2016).
[16] J. Xu, Q. Gu, and E. J. Mueller, Realizing the Haldane Phase with Bosons in Optical Lattices, Phys. Rev. Lett. **120**, 085301 (2018).
[17] F. A. An, E. J. Meier, J. Ang'ong'a, and B. Gadway, Correlated Dynamics in a Synthetic Lattice of Momentum States, Phys. Rev. Lett. **120**, 040407 (2018).
[18] X. Liu, F. Harper, and R. Roy, Chiral flow in one-dimensional Floquet topological insulators, Phys. Rev. B **98**, 165116 (2018).
[19] F. A. An, E. J. Meier, and B. Gadway, Direct observation of chiral currents and magnetic reflection in atomic flux lattices, Sci. Adv. **3**, e1602685 (2017).
[20] M. O. Scully, E. S. Fry, C. H. Raymond Ooi, and K. Wódkiewicz, Directed Spontaneous Emission from an Extended Ensemble of n Atoms: Timing Is Everything, Phys. Rev. Lett. **96**, 010501 (2006).
[21] See Supplemental Material at http://link.aps.org/supplemental/10.1103/PhysRevLett.122.023601 for details of the experimental set up and theoretical calculations, which includes Ref. [22].
[22] J. X. Zhang, H. T. Zhou, D. W. Wang, and S. Y. Zhu, Enhanced reflection via phase compensation from anomalous dispersion in atomic vapor, Phys. Rev. A **83**, 053841 (2011).
[23] M. Fleischhauer and M. D. Lukin, Dark-State Polaritons in Electromagnetically Induced Transparency, Phys. Rev. Lett. **84**, 5094 (2000).
[24] B. J. Feldman and M. S. Feld, Laser-induced line-narrowing effects in coupled Doppler-broadened transitions. 2. Standing-wave features, Phys. Rev. A **5**, 899 (1972).
[25] L. Zhang, L. Zhang, S. Niu, and X.-J. Liu, Dynamical classification of topological quantum phases, Sci. Bull. **63**, 1385 (2018).

[26] M. C. Rechtsman, J. M. Zeuner, Y. Plotnik, Y. Lumer, D. Podolsky, F. Dreisow, S. Nolte, M. Segev, and A. Szameit, Photonic Floquet topological insulators, Nature (London) **496**, 196 (2013).
[27] M. Hafezi, S. Mittal, J. Fan, A. Migdall, and J. M. Taylor, Imaging topological edge states in silicon photonics, Nat. Photonics **7**, 1001 (2013).
[28] Y. Zhang, Z. Wu, M. R. Belić, H. Zheng, Z. Wang, M. Xiao, and Y. Zhang, Photonic Floquet topological insulators in atomic ensembles, Laser Photonics Rev. **9**, 331 (2015).
[29] L. Xiao, X. Zhan, Z. H. Bian, K. K. Wang, X. Zhang, X. P. Wang, J. Li, K. Mochizuki, D. Kim, N. Kawakami, W. Yi, H. Obuse, B. C. Sanders, and P. Xue, Observation of topological edge states in parity-time-symmetric quantum walks, Nat. Phys. **13**, 1117 (2017).
[30] M. A. Bandres, S. Wittek, G. Harari, M. Parto, J. Ren, M. Segev, D. N. Christodoulides, and M. Khajavikhan, Topological insulator laser: Experiments, Science **359**, eaar4005 (2018).
[31] L. Yuan, Q. Lin, M. Xiao, and S. Fan, Synthetic dimension in photonics, Optica **5**, 1396 (2018).
[32] F. D. M. Haldane and S. Raghu, Possible Realization of Directional Optical Waveguides in Photonic Crystals with Broken Time-Reversal Symmetry, Phys. Rev. Lett. **100**, 013904 (2008).
[33] Z. Wu, L. Zhang, W. Sun, X. T. Xu, B. Z. Wang, S. C. Ji, Y. J. Deng, S. Chen, X. J. Liu, and J. W. Pan, Realization of two-dimensional spin-orbit coupling for Bose-Einstein condensates, Science **354**, 83 (2016).
[34] L. Huang, Z. Meng, P. Wang, P. Peng, S.-L. Zhang, L. Chen, D. Li, Q. Zhou, and J. Zhang, Experimental realization of two-dimensional synthetic spin–orbit coupling in ultracold Fermi gases, Nat. Phys. **12**, 540 (2016).
[35] F. D. M. Haldane, Model for a Quantum Hall Effect without Landau Levels: Condensed-Matter Realization of the "Parity Anomaly", Phys. Rev. Lett. **61**, 2015 (1988).
[36] G. Jotzu, M. Messer, R. Desbuquois, M. Lebrat, T. Uehlinger, D. Greif, and T. Esslinger, Experimental realization of the topological Haldane model with ultracold fermions, Nature (London) **515**, 237 (2014).
[37] T. Peyronel, O. Firstenberg, Q. Y. Liang, S. Hofferberth, A. V. Gorshkov, T. Pohl, M. D. Lukin, and V. Vuletic, Quantum nonlinear optics with single photons enabled by strongly interacting atoms, Nature (London) **488**, 57 (2012).
[38] F. Ripka, Y.-H. Chen, R. Löw, and T. Pfau, Rydberg polaritons in a thermal vapor, Phys. Rev. A **93**, 053429 (2016).
[39] S. Greschner and T. Vekua, Vortex-Hole Duality: A Unified Picture of Weak- and Strong-Coupling Regimes of Bosonic Ladders with Flux, Phys. Rev. Lett. **119**, 073401 (2017).
[40] Z. Lin, H. Ramezani, T. Eichelkraut, T. Kottos, H. Cao, and D. N. Christodoulides, Unidirectional Invisibility Induced by $\mathcal{PT}$-Symmetric Periodic Structures, Phys. Rev. Lett. **106**, 213901 (2011).
[41] A. Regensburger, C. Bersch, M.-A. Miri, G. Onishchukov, D. N. Christodoulides, and U. Peschel, Parity-time synthetic photonic lattices, Nature (London) **488**, 167 (2012).
[42] J.-H. Wu, M. Artoni, and G. C. La Rocca, Non-Hermitian Degeneracies and Unidirectional Reflectionless Atomic Lattices, Phys. Rev. Lett. **113**, 123004 (2014).
[43] Y. Huang, Y. Shen, C. Min, S. Fan, and G. Veronis, Unidirectional reflectionless light propagation at exceptional points, Nanophotonics **6**, 977 (2017).
[44] L. Feng, R. El-Ganainy, and L. Ge, Non-Hermitian photonics based on parity-time symmetry, Nat. Photonics **11**, 752 (2017).
[45] D.-W. Wang, H.-T. Zhou, M.-J. Guo, J.-X. Zhang, J. Evers, and S.-Y. Zhu, Optical Diode Made from a Moving Photonic Crystal, Phys. Rev. Lett. **110**, 093901 (2013).